Supporting Information

High performance solid-state thermoelectric energy conversion via inorganic metal halide perovskites under tailored mechanical deformation

Lifu Yan[a], Lingling Zhao[a,*], Guiting Yang[b], Shichao Liu[b], Yang Liu[b], Shangchao Lin[c,*]

[a]National Engineering Research Center of Turbo-Generator Vibration, School of Energy and Environment, Southeast University, Nanjing 210096, China

[b]State Key Laboratory of Space Power-sources Technology, Shanghai Institute of Space Power-Sources, Shanghai 200245, China

[c]Key Laboratory for Power Machinery and Engineering of Ministry of Education, School of Mechanical Engineering, Shanghai Jiao Tong University, Shanghai 200240, China

*Corresponding author's contact information:

Lingling Zhao, E-mail: zhao_lingling@seu.edu.cn

Shangchao Lin, E-mail: shangchaolin@sjtu.edu.cn

Table S1 The lattice constants and the space group of the two representative polymorphic configurations after DFT geometry optimization. The equivalent lattice constants along *X* are determined as half of the supercell dimension along *X*

Perovskites	Equivalent Lattice Constant along *X*/Å	Super cll Lattice Constants/Å			Space group
		X	*Y*	*Z*	
$CsPbI_3$	6.383	12.766	6.383	6.383	Pm-3m
$CsPbIBr_2$	6.408	12.815	5.987	5.987	P4/mmm

Supplementary Notes on Table S1:

We can see that the equivalent lattice constant along *X* of $CsPbI_3$ is the same as those along *Y* and *Z* directions. However, the equivalent lattice constant along *X* of $CsPbIBr_2$ is much larger than the lattice constants along *Y* and *Z* directions because of the larger van der Waals radii of the I atom, which leads to the electronic band structure splitting (**Fig. 3**) and even the anisotropic transport properties. For example, the Pauling van der Waals radius of I atom is 2.15 Å, which is larger than that of Br atom (1.95 Å). Specifically, there are two I atoms along *X*, two Br atoms along *Y*, and two Br atoms along *Z* directions in $CsPbIBr_2$.

Table S2 The mechanical properties of the two representative polymorphic configurations under mechanical deformation effect (strain-free and extensive strain +2%) along *X* direction using VRH (Voigt-Reuss-Hill) approximation

Averaging	$CsPbI_3$		$CsPbIBr_2$	
scheme (Hill)	Strain-free	*X* +2%	Strain-free	*X* +2%
Young's modulus	22.00 GPa	20.80 GPa	26.05 GPa	24.89 GPa
Bulk modulus	17.73 GPa	16.46 GPa	21.10 GPa	19.72 GPa
Shear modulus	8.506 GPa	8.064 GPa	10.06 GPa	9.650 GPa
Poisson ratio	0.293	0.289	0.294	0.290

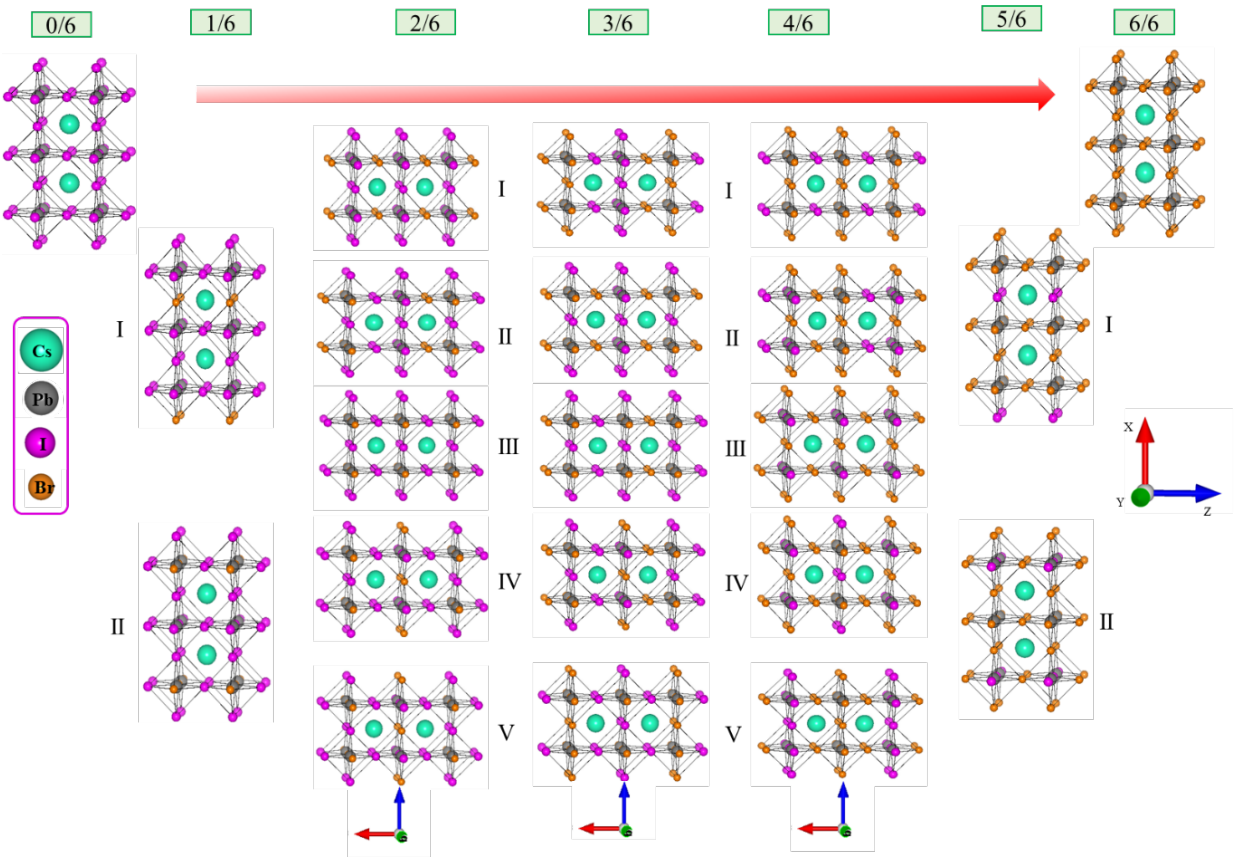

Fig. S1 The DFT-optimized supercell structures of the 21 halide perovskites $CsPb(I_{1-x}Br_x)_3$.

Supplementary Notes on Fig. S1:

The halogen element substitution (from I to Br atom) in the starting pseudo-cubic supercell with a 2 × 1 × 1 expansion of the cubic unit cell of $CsPbI_3$ produces a total of 64 polymorphs. After considering symmetry, the 64 polymorphs reduce to 21 symmetry-nonequivalent polymorphic structures. At a fixed Br composition (x = 0/6 to 6/6), each polymorph can be denoted by I, II, III, IV, and V, *i.e.*, 4/6-I represents the first polymorph at a Br composition x = 4/6. Here, **Fig. S1** shows a complete set of structures of the optimized $CsPb(I_{1-x}Br_x)_3$ from x = 1/6 to 5/6.

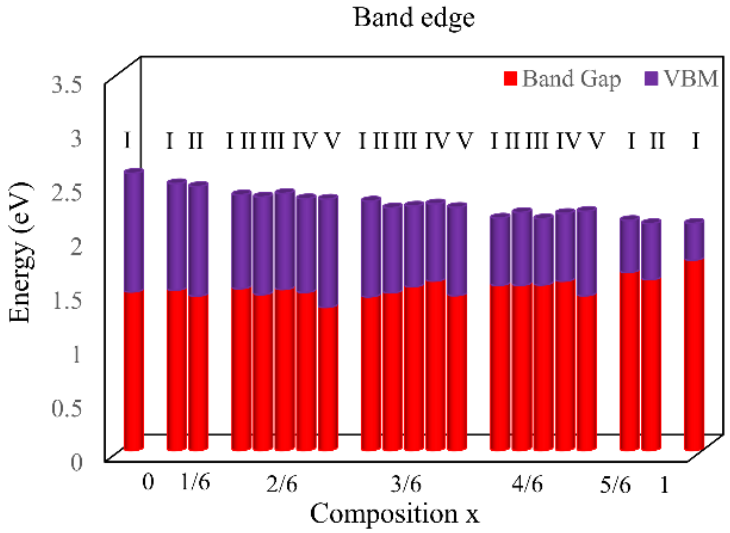

Fig. S2 Band edges (CBM and VBM) and gaps of pure and polymorphic mixed halide perovskites without mechanical deformation.

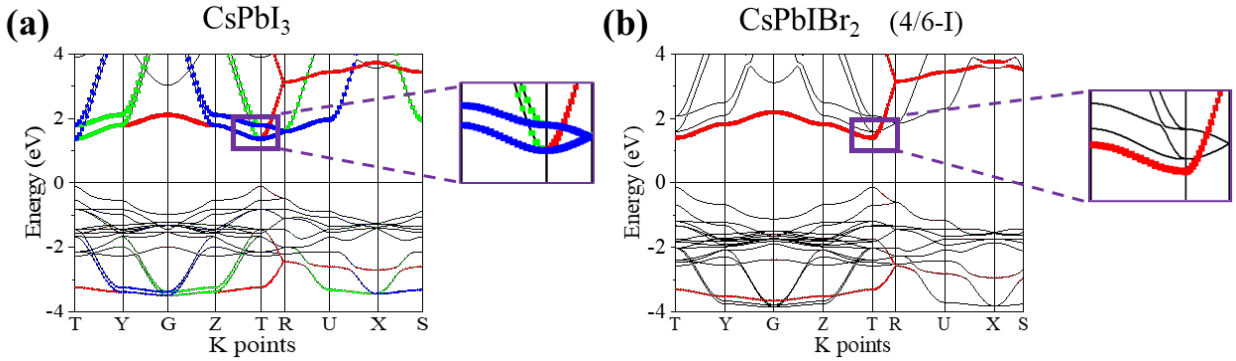

Fig. S3 Electronic structures of the (a) pure $CsPbI_3$ and mixed (b) $CsPbIBr_2$ perovskites without mechanical deformation.

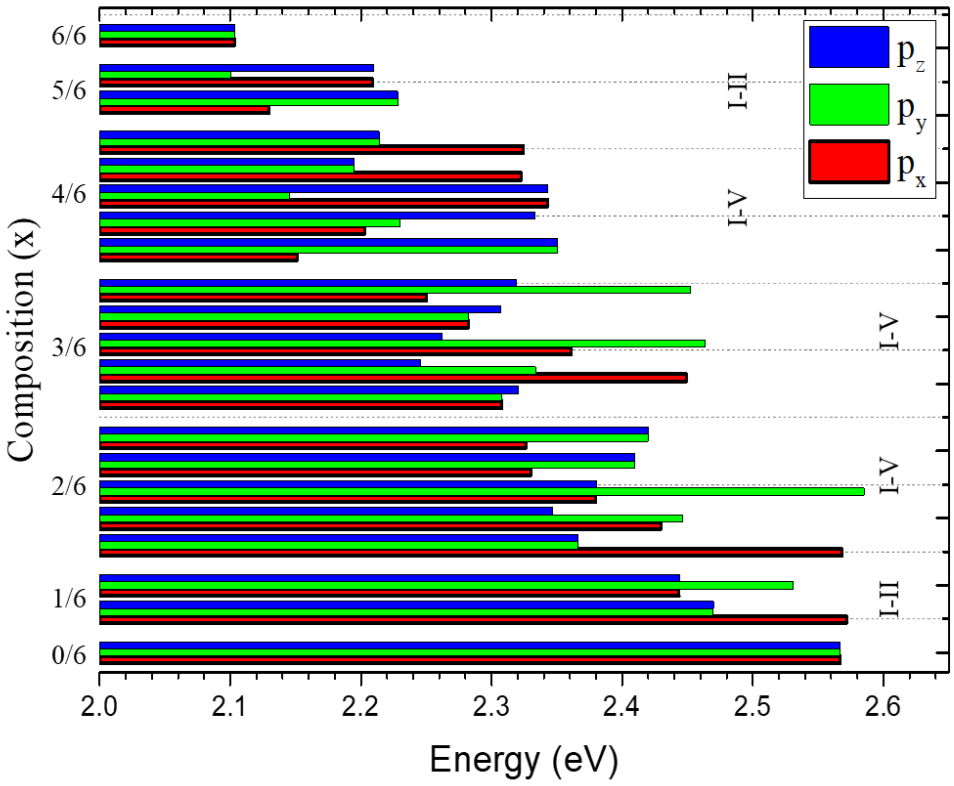

Fig. S4 The energy levels of the split Pb-6p_x, 6p_y, and 6p_z orbitals of the 21 polymorphic mixed halide perovskites $CsPb(I_{1-x}Br_x)_3$ considered here without mechanical deformation.

Supplementary Notes on Fig. S4:

The direction of the intrinsic strain is traceable based on the detailed halogen arrangement in each polymorph. For the pseudo-cubic supercell considered here, the intrinsic strain may exist along one, two, or three directions. The $CsPb(I_{1-x}Br_x)_3$ polymorphs can be categorized into three groups based on different splitting characters of the Pb-6p orbitals without strains: (i) energy levels of 6p_x, 6p_y, and 6p_z orbitals remain the same (three-fold degenerated), including 0/6, 6/6 (pure halide perovskites), 3/6-I, and 3/6-IV (one halogen atom substitution along each of the X, Y, or Z dimension) polymorphs; (ii) energy level of only one orbital 6p_x/6p_y/6p_z shifts, while the other two almost remain the same as being two-fold degenerated, including 1/6, 2/6, 4/6, and 5/6 polymorphs; and (iii) all three orbitals split, including 3/6-II, 3/6-III, and 3/6-V polymorphs. In the main

manuscript, the three-fold degenerated $CsPbI_3$ and two-fold degenerated $CsPbIBr_2$ under uniaxial strain effect are investigated. While in the Supplementary Information, we are focusing on one three-orbitals split case (3/6-II) and another one two-fold degenerated case with the two-fold degenerated orbital as CBM (1/6-I).

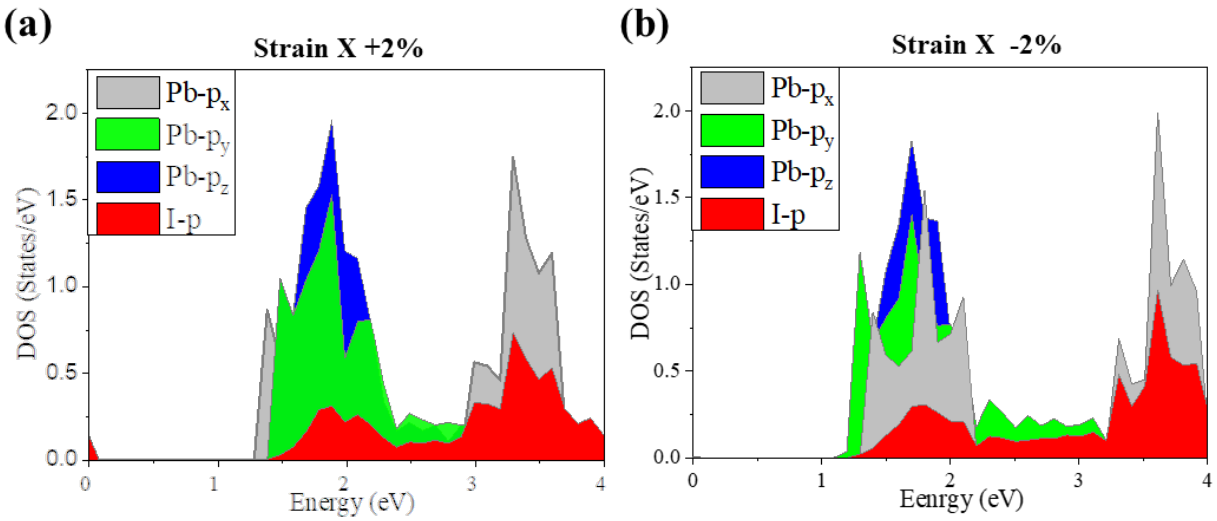

Fig. S5 Projected DOS of $CsPbI_3$: (a) under positive strain, and (b) under negative strain along X axis.

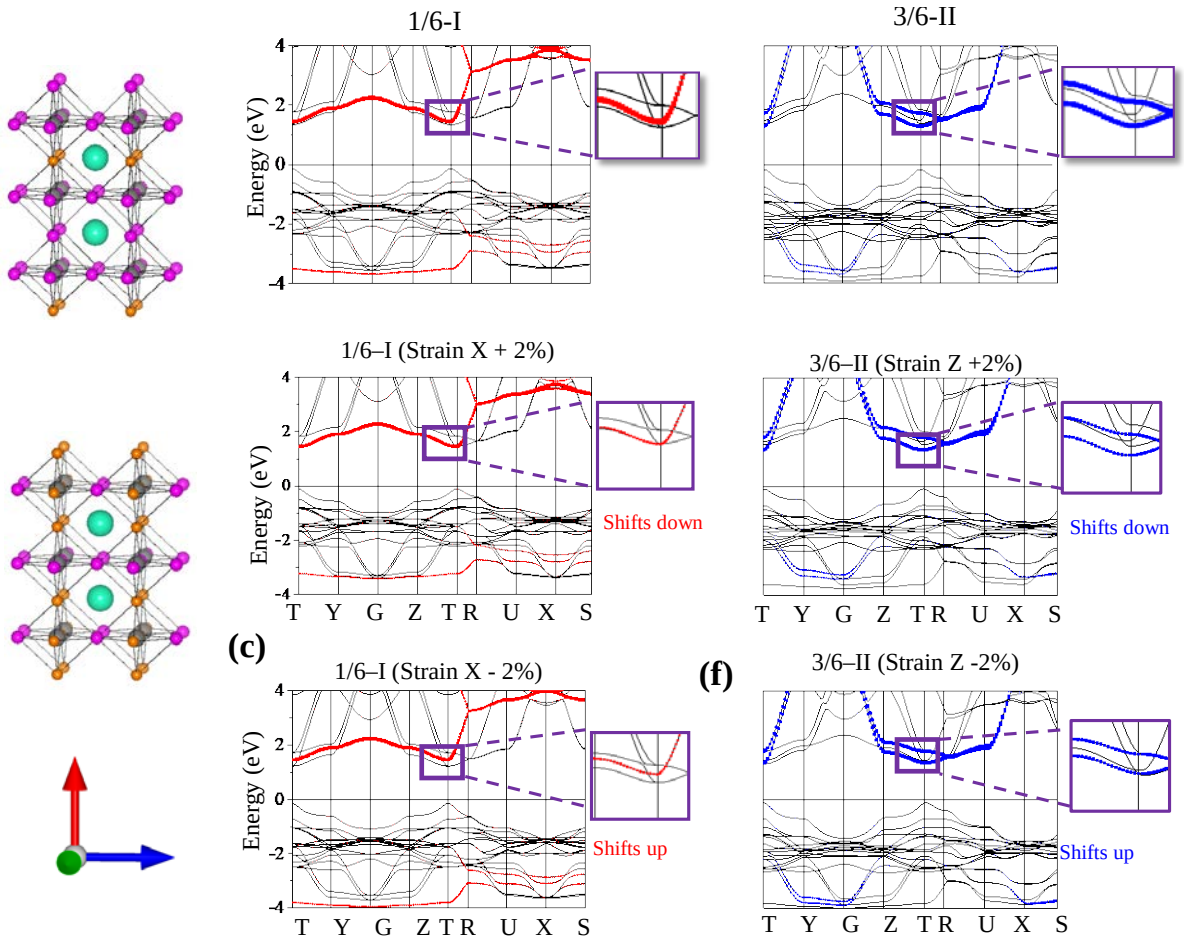

Fig. S6 Electronic structures of 1/6-I along *X* direction under (a) no strain (b) positive +2% strain, and (c) negative -2% strain. Electronic structures of 3/6-II along *Z* direction under (d) no strain (e) positive +2% strain, and (f) negative -2% strain.

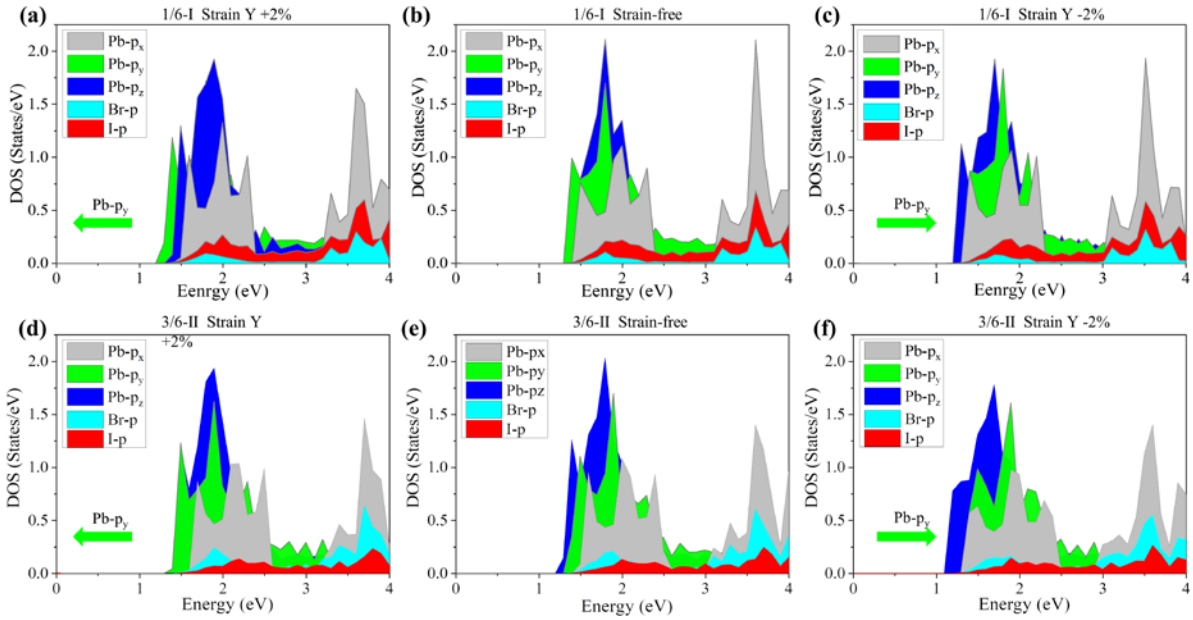

Fig. S7 The strain effect along *Y* direction on the projected DOS of 1/6-I: (a) under positive strain, (b) no strain, and (c) negative strain. The strain effect along *Y* direction on the projected DOS of 3/6-II: (d) under positive strain, (e) no strain, and (f) negative strain.

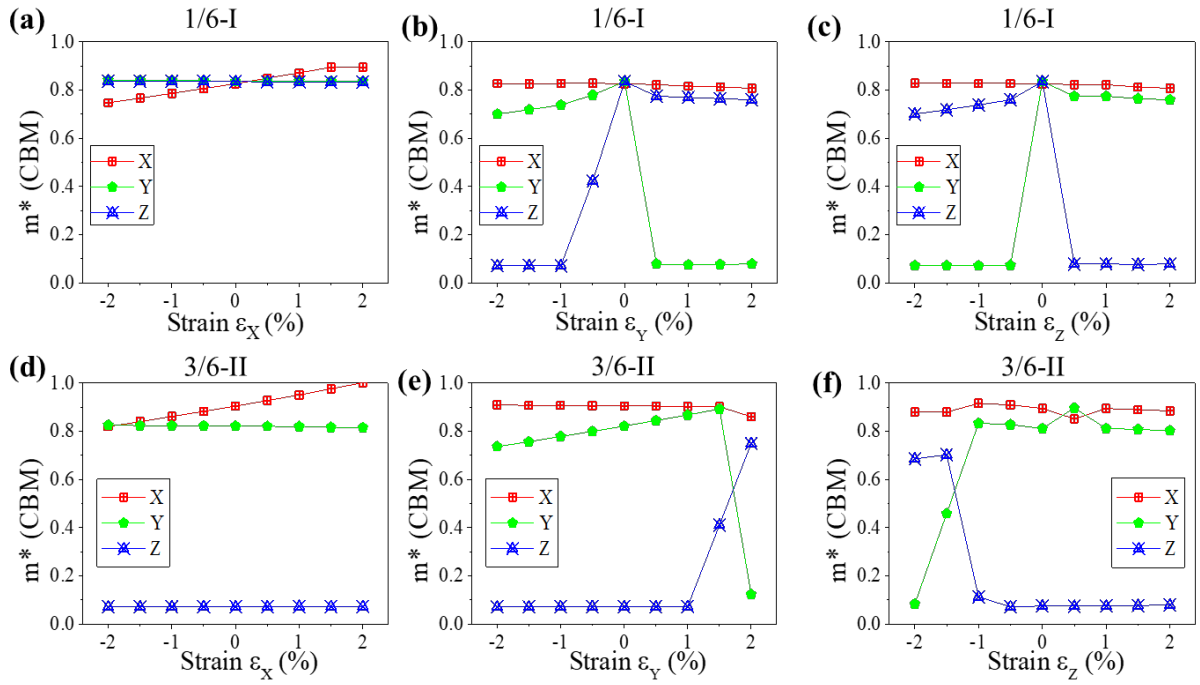

Fig. S8 The strain effect on the effective masses of 1/6-I along: (a) *X* direction, (b) *Y* direction, and (c) *Z* direction. The strain effect on the effective masses of 3/6-II along: (a) *X* direction, (b) *Y* direction, and (c) *Z* direction.

Supplementary Notes on Fig. S6-S8:

Interestingly, the carrier effective mass will suddenly change under strain if the mechanical deformation effect can overcome the symmetry-breaking effect to reconstruct the CBM. Taking 1/6-I for example, one Br atom substitutes one I atom along the *X* axis would result in an intrinsic compressive strain along the *X* direction, causing the energy of the Pb-6p_x orbital to shift up, while that of the 6p_y and 6p_z orbitals almost remain the same. As shown in **Fig. S6,** for 1/6-I, a 2% strain along *X* direction (the same as the original local residue strain direction upon halogen mixing) fails to cancel out the Pb-6p_x orbital splitting caused by symmetry-breaking, leading to small (without

sudden transitions) changes to the electron effective masses m_x* or m_y* compared to the original strain-free levels, respectively. However, as shown in **Fig. S8** for 3/6-II, there is a sudden change of the effective mass at -1.5% strain along Z for the 3/6-II perovskite, indicating that the –1.5% strain along Z would overcome the original residue strain effect, which is expected to significantly impact transport properties. When the directions of the residue strain and the external strain are different (orthogonal), taking 1/6-I for example, even a small strain of 0.5% along *Y* can shift the Pb-6p_y orbital down and destroy the two-fold degenerated (6p_y/6p_z) states. As the Pb-6p_y orbital becomes the new CBM, it leads to a giant decrease in the effective mass along *Y* (see **Fig. 8**) with large enhancement in the transport properties, as will be discussed in the next section. Furthermore, it should be noted that a small strain of –0.5% along *Y* in 1/6-I perovskite can also destroy the two-fold degenerated states (6p_y/6p_z), as the Pb-6p_y orbital shifts up and leaves Pb-6p_z orbital become the new CBM, leading to a giant decrease in the effective mass along *Z* direction.

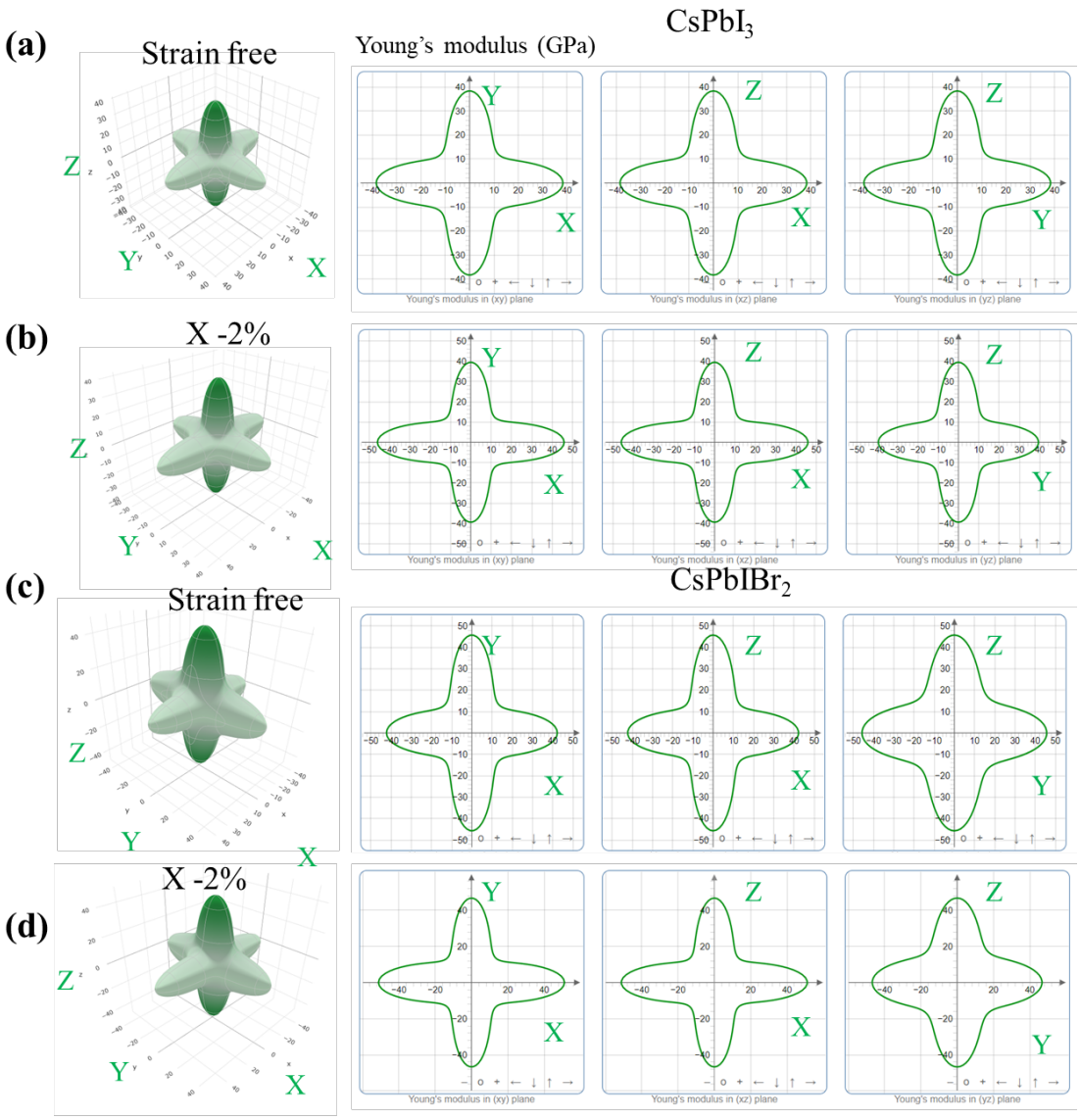

Fig. S9 The 3D anisotropic and the projected 2D Young's modulus of the pure $CsPbI_3$ perovskite under (a) strain free and (b) –2% strain along X direction, as well as the 3D anisotropic and the projected 2D Young's modulus of the mixed $CsPbIBr_2$ perovskite under (c) strain free and (d) –2% strain along *X* direction.

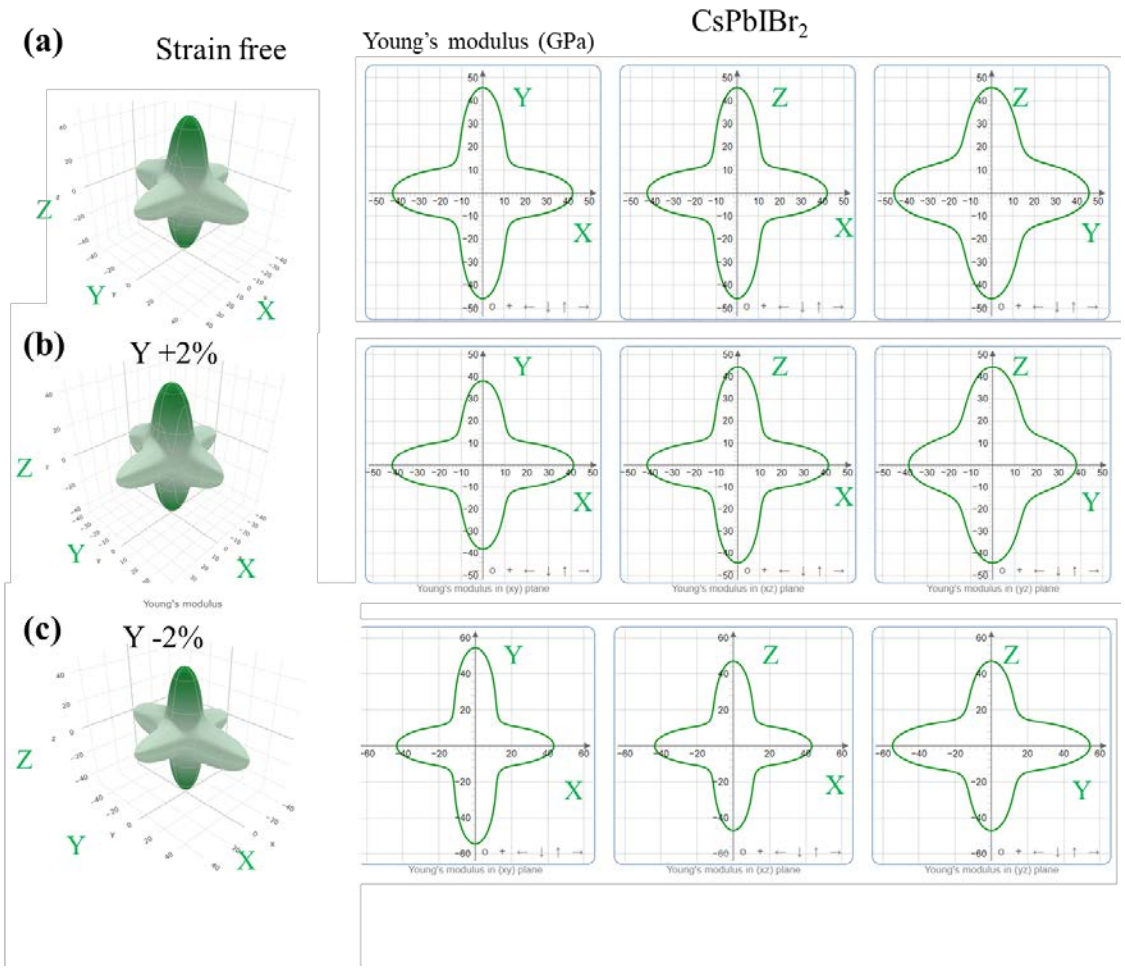

Fig. S10 The 3D anisotropic and the projected 2D Young's modulus of the mixed $CsPbIBr_2$ perovskite under (a) strain free, (b) +2% strain along *Y* direction, and (c) –2% strain along *Y* direction.

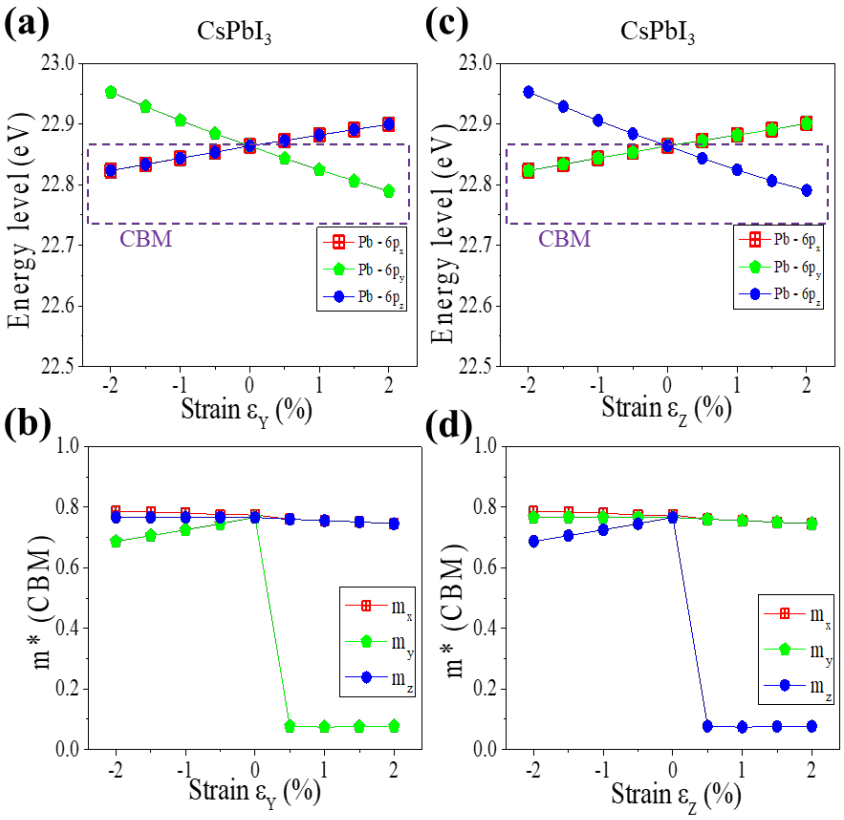

Fig. S11. The energy levels of the $6p_x$, $6p_y$, and $6p_z$ orbitals of Pb and anisotropic electron effective masses m^* at the CBM when strain applies, (a-b) along *Y* direction, (c-d) along *Z* direction.

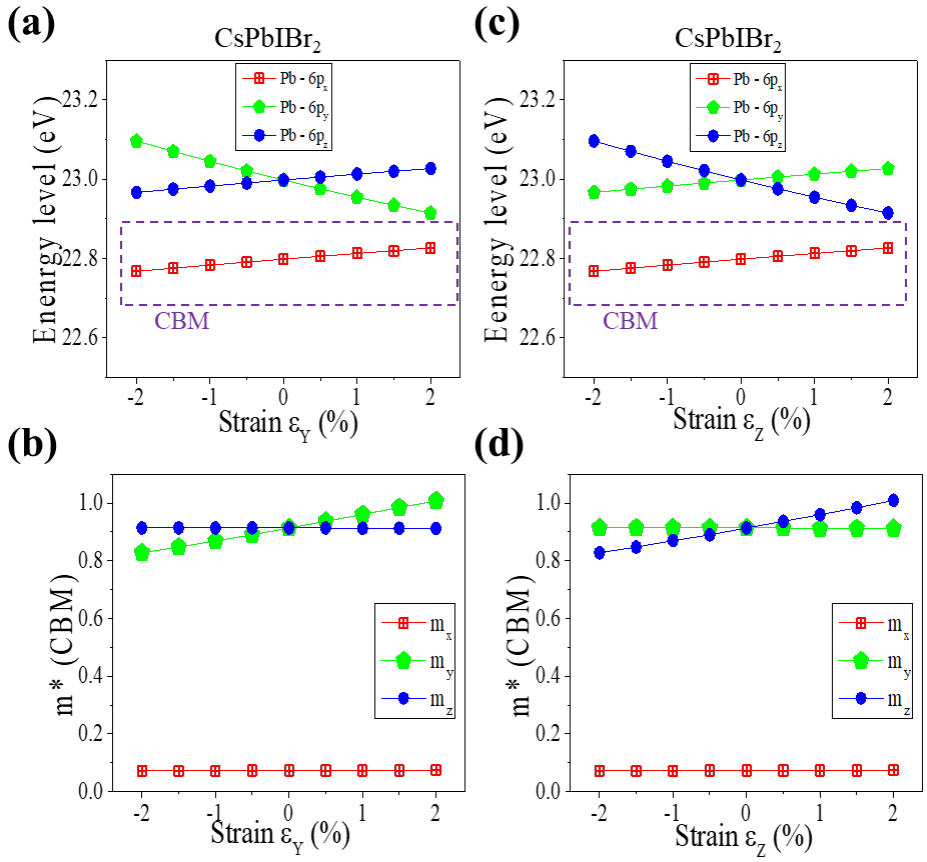

Fig. S12. The energy levels of the $6p_x$, $6p_y$, and $6p_z$ orbitals of Pb and anisotropic electron effective masses m^* at the CBM when strain applies, (a-b) along *Y* direction, (c-d) along *Z* direction.

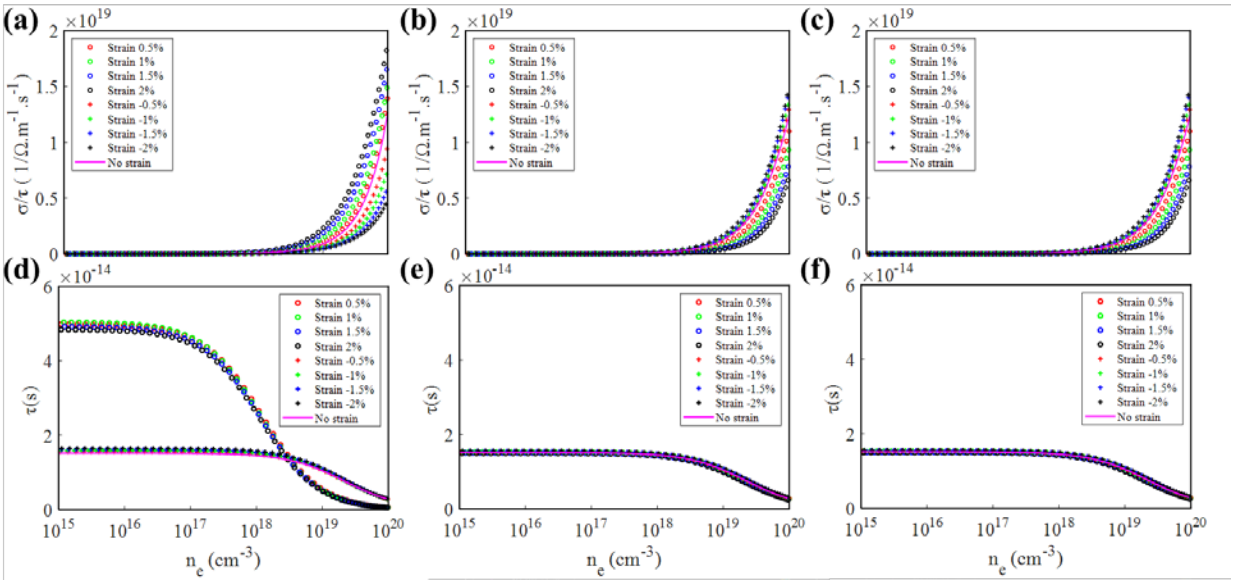

Fig.13. Carrier relaxation time-normalized anisotropic electric conductivity and anisotropic relaxation time of $CsPbI_3$ at 300 K as a function of carrier concentration n_e, when external strains are applied along different directions.

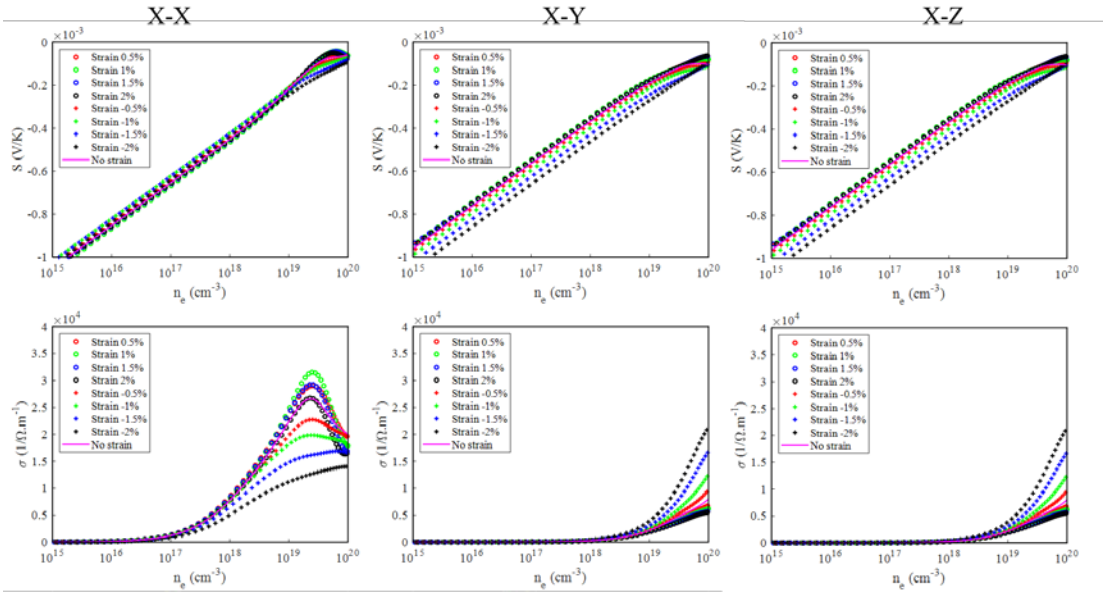

Fig.14. The transport properties of $CsPbIBr_2$ (including the Seebeck coefficient and electric conductivity) as a function of carrier concentration n_e, when external strains are applied along *X* direction.

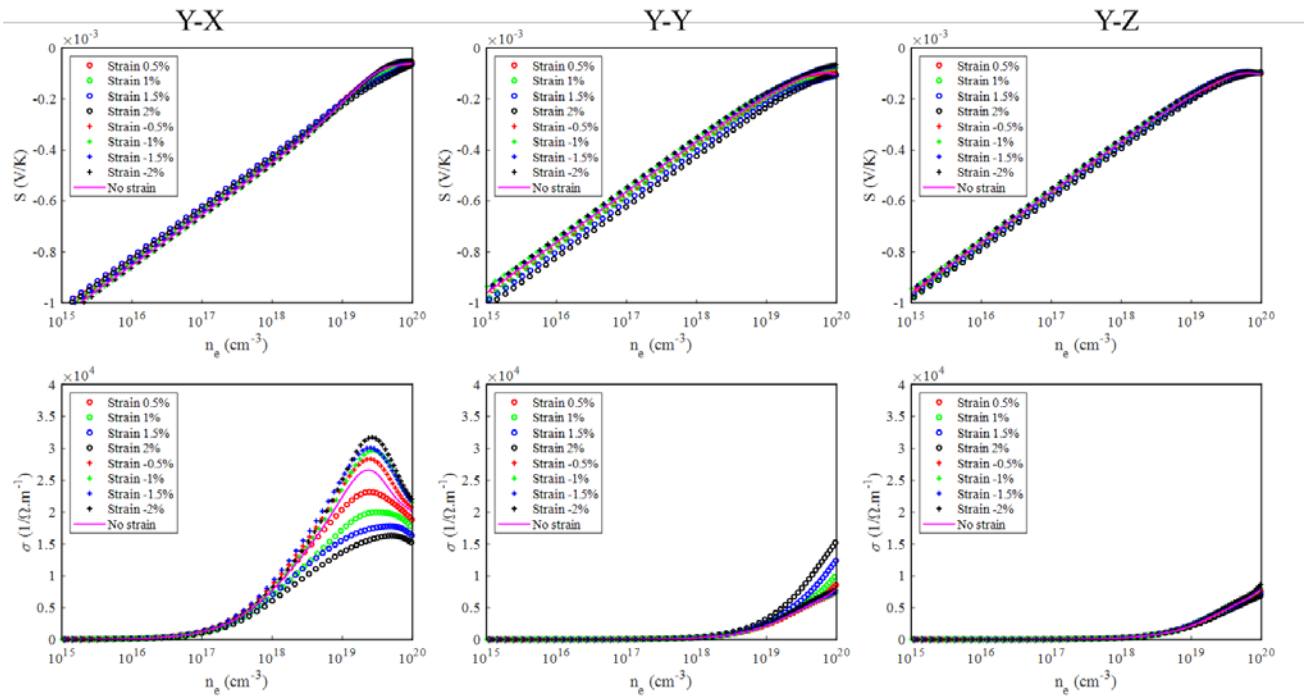

Fig.15. The transport properties of $CsPbIBr_2$ (including the Seebeck coefficient and electric conductivity) as a function of carrier concentration n_e, when external strains are applied along *Y* direction.

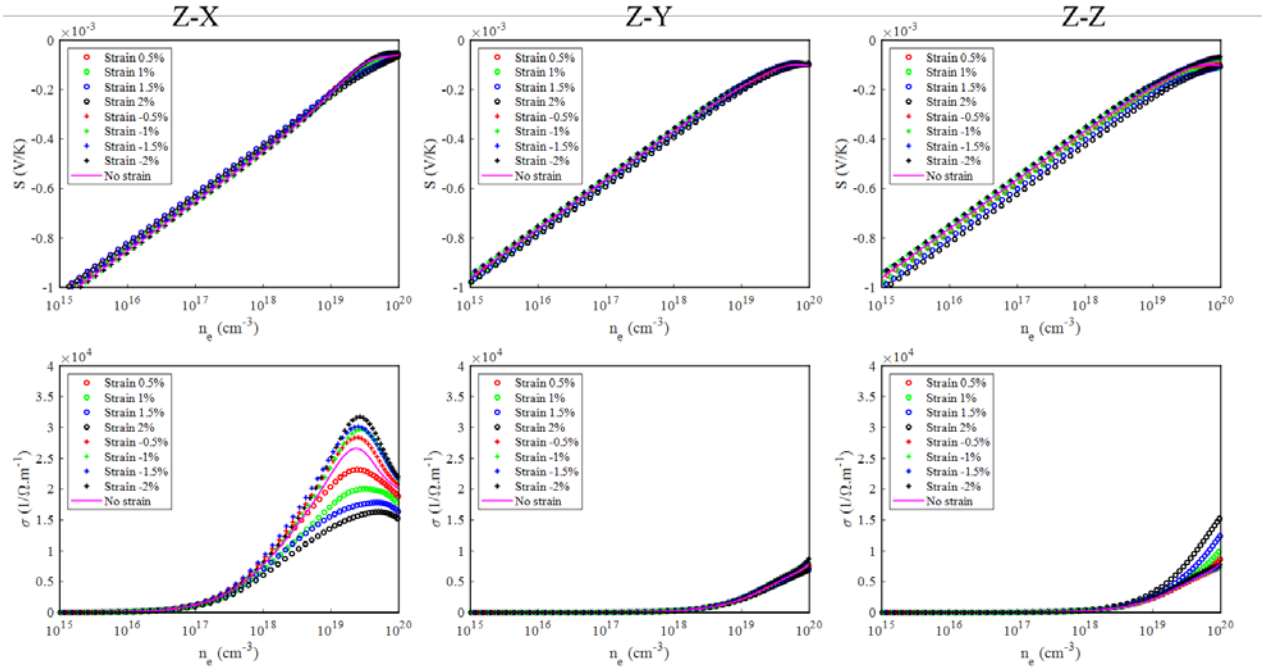

Fig.16. The transport properties of $CsPbIBr_2$ (including the Seebeck coefficient and electric conductivity) as a function of carrier concentration n_e, when external strains are applied along *Z* direction.

Supplementary Notes on Fig. S14-S16:

For the $CsPbIBr_2$, the Pb-6p$_x$ orbital shifts down, while the other two remain at the same energy level without strains, such that thermoelectric transport properties along these two directions are similar (We can see that *Y-X/Y/Z* and *Z-X/Z/Y* cases are similar to each other from **Fig. S15, S16**). In addition, the strain effect is not strong enough to cancel out the symmetry-breaking effect completely, and the Pb-6p$_x$ orbital remains the CBM. Therefore, the transport properties of $CsPbIBr_2$ do not change much under strains. The magnitudes of S and σ vary slightly as the extensive/compressive strain increases, attributed to the combined changes in the degeneracy and the effective mass.

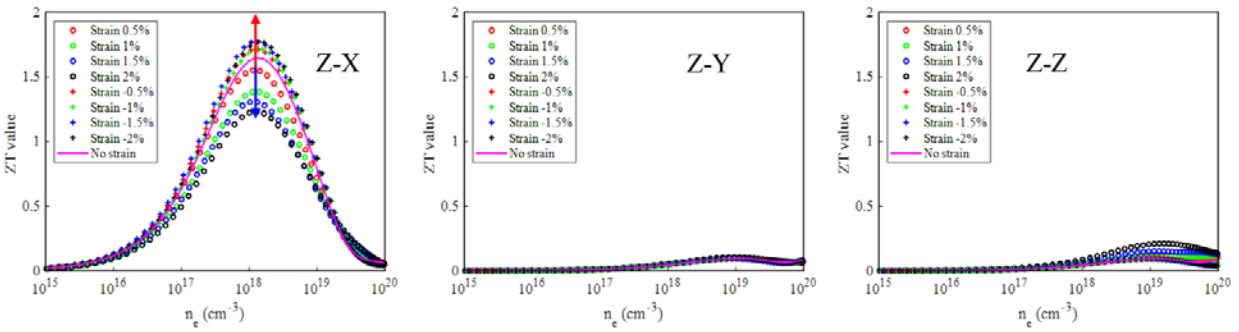

Fig.17. The *ZT* values of the $CsPbIBr_2$ as a function of carrier concentration n_e, when external strains are applied along *Z* direction.

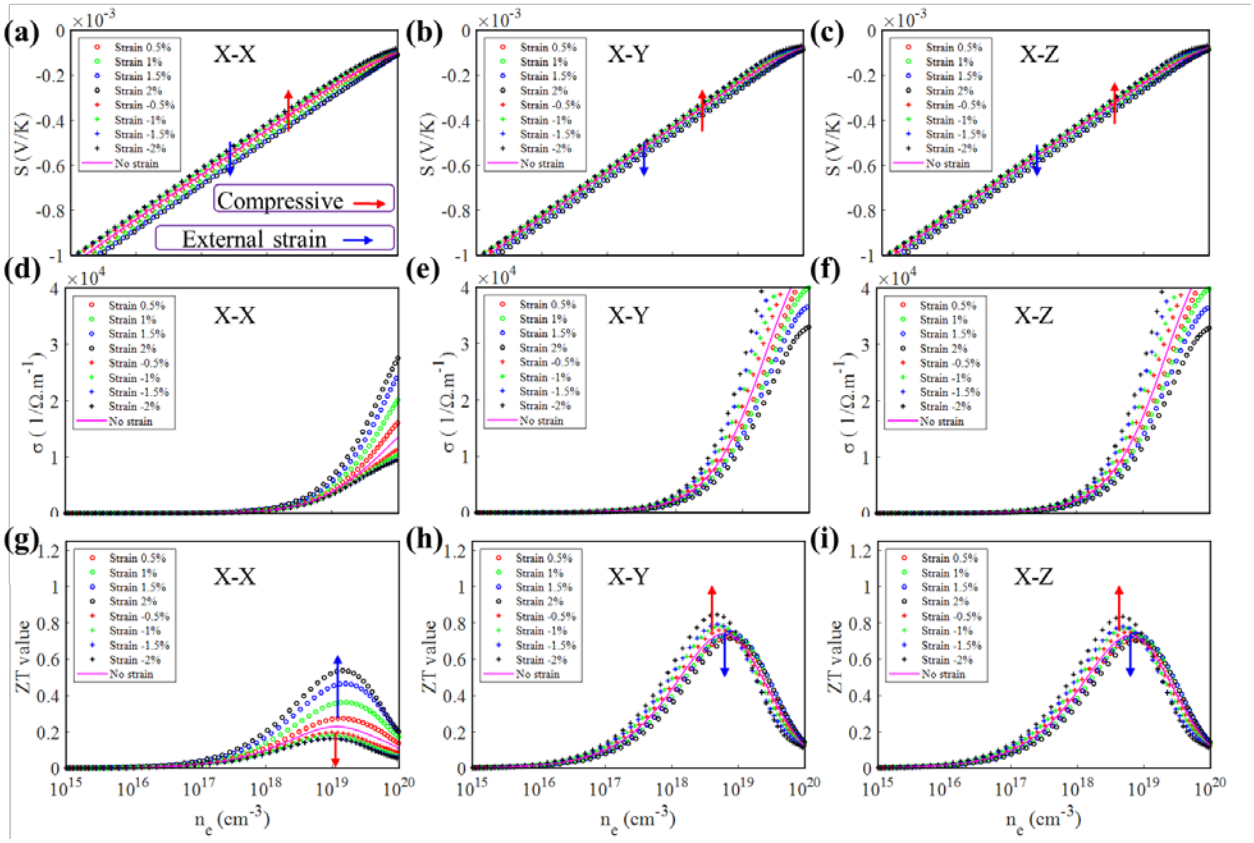

Fig. S18 Anisotropic transport properties of mixed halide perovskites at 300 K (taking the 1/6-I polymorph for example) as a function of carrier concentration n_e, when external strains are applied along *X* direction.

Supplementary Notes on Fig. S18:

For the second group of $CsPb(I_{1-x}Br_x)_3$, only one Pb-6p orbital shifts, while the other two remain at the same energy level without strains, such that transport properties along these two directions are similar. Therefore, we show the strain effect only along two directions and presume that the third one is similar. Taking 1/6-I for example (*Y-X/Y/Z* and *Z-X/Z/Y* cases are similar to each other), the magnitude of *S* increases slightly as the extensive strain increases along *X*, attributed to the increased level of degeneracy: from two-fold in **Fig. S6(a)** to three-fold in **Fig. S6(b)** for the Pb-6p orbitals. In this group of $CsPb(I_{1-x}Br_x)_3$, extensive strains shift down the $6p_x$ orbital and weaken the symmetry-breaking effect, however, the strain effect is not strong enough to cancel out the symmetry-breaking effect completely. As shown in **Fig. S18**, σ increases slightly under extensive strains, leading to increases in *ZT* values (from about 0.2 to 0.5) as strain increases to 2% along *X-X* (see **Fig. S18g**). Along *X-Y* and *X-Z*, the transport properties are only slightly affected by the strain effect.

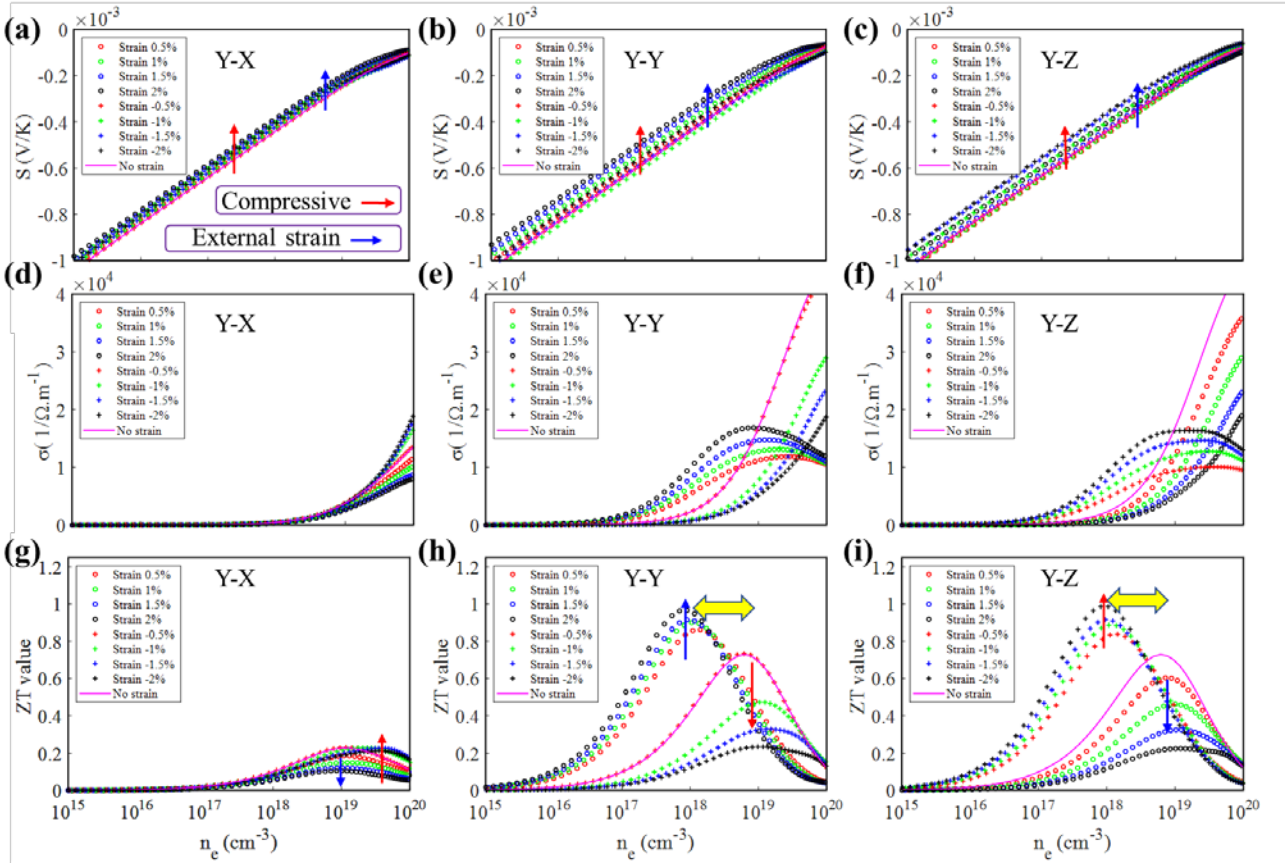

Fig. S19 Anisotropic transport properties of mixed halide perovskites at 300 K (taking the 1/6-I polymorph for example) as a function of carrier concentration n_e, when external strains are applied along *Y* direction.

Supplementary Notes on Fig. S19:

Interestingly, when strain is applied along *Y* in the 1/6-I polymorph, the Pb-6p$_y$ orbital shifts up or down significantly, destroying the original two-fold degeneracy of Pb-6p$_y$ and Pb-6p$_z$ **(Fig. S7)** and decreasing the magnitude of *S* as the magnitude of strain increases (**Fig. S19**). The downward shift of the Pb-6p$_y$ orbital (becoming the new CBM) under extensive strains along *Y* would reduce the effective mass along *Y* dramatically, while the effective mass along *Z* (downward shift of the Pb-

$6p_z$ orbital that becomes the new CBM) decreases sharply, but under compressive strain along *Y* **(**see **Fig. S19)**. This leads to significant increases in σ along *Y* (*Z*) at lower carrier concentrations when increasing extensive (compressive) strain (**Fig. S19d-f)**. Therefore, the maximum *ZT* value for *Y*-*Y* increases from 0.7 without strain to 1.0 at a 2% strain, while the maximum *ZT* value for *Y*-*Z* increases also from 0.7 without strains to 1.0 at a –2% strain (**Fig. S19g-i**). This also leads to a reduction of the corresponding optimal carrier concentration by one order of magnitude (**Fig. S19g-i**).

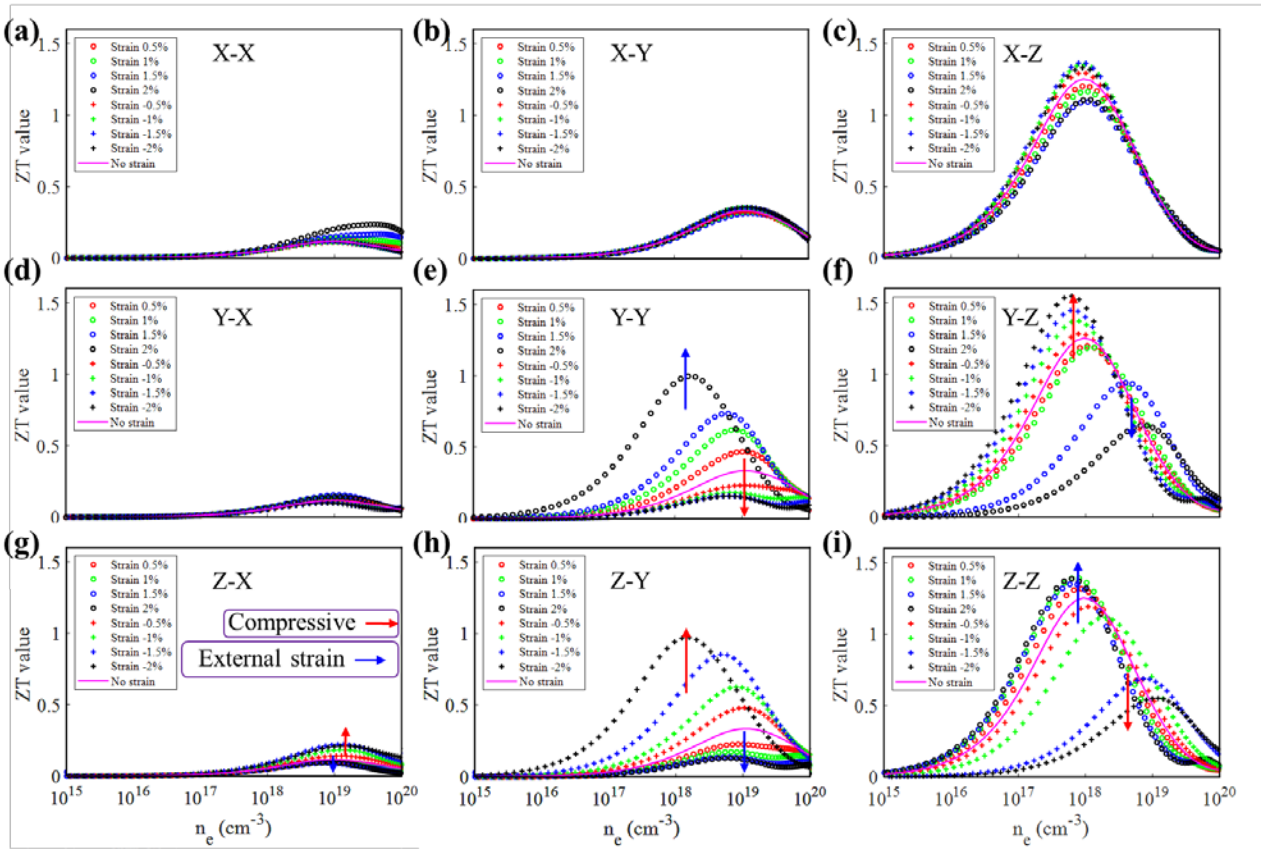

Fig. S20 Anisotropic *ZT* values of mixed halide perovskites at 300 K (taking the 3/6-II polymorph for example) as a function of carrier concentration n_e, when external strains are applied along different directions.

Supplementary Notes on Fig. S20:

In the third group of $CsPb(I_{1-x}Br_x)_3$ with completely non-degenerated Pb-6p orbitals, such as the 3/6-II polymorph, the split orbital energy levels follow the trend: Pb-$6p_x$ > $6p_y$ > $6p_z$ (**Fig. S6**). Therefore, anisotropic transport properties are observed when external strains are applied along different dimensions. Since the external strain-induced variations in *S* and σ follow the same trend mentioned above (resulting from orbital shifts), we only show the computed anisotropic *ZT* values

as a function of carrier concentration n_e when stains are applied along different directions. As shown in **Fig. S20,** the *ZT* values along *X* exhibit little strain effect, regardless of the strain direction, because the energy level of $6p_x$ is way above the CBM and insensitive to the strain effect. As shown in **Fig. S20e**, the optimal carrier concentration to achieve the maximum *ZT* along *Y* is reduced by more than one order of magnitude under a 2% strain along *Y*, compared to the strain-free and compressive strain cases. On the other hand, as shown in **Fig. S20f**, the optimal carrier concentration to achieve the maximum *ZT* along *Z* is instead increased by almost one order of magnitude under a 2% strain along *Y*, compared to the strain-free and compressive strain cases. These are due to the fact that the energy level of the $6p_y$ orbital shifts down and crosses that of the $6p_z$ orbital to become the new CBM when extensive strains are applied along *Y* (see **Fig. S6d**), which is consistent with the computed effective mass (see **Fig. S8)**. This also applies similarly to *ZT* values under compressive strains along *Z* (**Fig. S20)**, in which the energy level of the $6p_z$ orbital also shifts down and crosses that of the $6p_y$ orbital to become the new CBM.

SUPPLEMENTARY METHODS

Carrier Relaxation Time Calculations

In this paper, the deformation potential theory, Brooks-Herring approach, and Fröhlich model were used to describe the scattering processes between charge carriers with longitudinal acoustic (LA) phonons, ionized impurities, and polar longitudinal optical (LO) phonons, respectively, in order to estimate the carrier relaxation time τ. While LA phonon and ionized impurity scatterings are very common in most of the thermoelectric materials, the inclusion of LO phonon scattering reflects the fact that halide perovskites are polar materials. It has been verified that in the charge carrier relaxation process, the major contribution to electron-phonon coupling comes from the polar longitudinal optical phonons in $MAPbI_3$[1].

Firstly, the deformation potential theory was used to describe the scattering process between charge carriers and LA phonons[2-6], and a simplified form for τ_{ac} can be expressed as follows:

$$\frac{1}{\tau_{ac}} = \frac{\sqrt{2}\, m^{3/2}}{\pi\hbar^4} \frac{k_{\mathrm{B}} T E_{\mathrm{DP}}^2}{\rho v^2} E^{1/2} \tag{1}$$

where, $m = (m_x^* m_y^* m_z^*)^{1/3}$ is the averaged effective mass of the carrier, k_{B} is the Boltzmann constant, E_{DP} is the deformation potential constant, E is the electron energy at VBM/CBM, $\hbar$ is the reduced Planck constant, ρ the mass density, and v is the average sound velocity.

Secondly, the Brooks-Herring approach was used to model the ionized impurity scattering process[7].

$$\frac{1}{\tau_{\mathrm{imp}}} = \frac{\pi}{m^{*1/2}} \frac{{Z_{ion}}^2 e^4 N}{\varepsilon^2 (2E)^{3/2}} \left[\ln(1+b) - \frac{b}{1+b}\right] \tag{2}$$

where, Z_{ion}= 1 is the charge of the impurity, ε is the permittivity, N is the ionized impurity concentration, which was chosen to be equal to the carrier concentration according to the full ionization assumption in earlier work[8], $b = \frac{8mE}{\hbar^2\beta_s^2}$, $\beta_s^2 = L_D^{-2} = \frac{N_0 e^2}{\varepsilon k_B T}$, $N_0 = \frac{1}{\sqrt{2}\hbar^3}\left(\frac{mk_BT}{\pi}\right)^{\frac{3}{2}}\mathcal{F}_{1/2}(\eta)$ is the free carrier concentration, and here, $\eta = \frac{E_F}{k_B T}$, $\mathcal{F}_j(y_0) = \frac{1}{\Gamma(j+1)}\int_0^\infty \frac{y^j dy}{1+\exp(y-y_0)}$.

Thirdly, for polar optical scattering (LO phonon scattering), which was first investigated by Fröhlich[9], and the relaxation time can be expressed as follows[10, 11]:

$$\frac{1}{\tau_{pop}} = \frac{e^2}{4\pi\hbar}\left(\frac{2\omega m^*}{\hbar}\right)^{\frac{1}{2}}\left(\frac{1}{\varepsilon_\infty}-\frac{1}{\varepsilon_s}\right)[n(\omega)+1]\frac{f_0(E+\hbar\omega)}{f_0(E)}\left(\frac{\hbar\omega}{E}\right)^{\frac{1}{2}}\sinh^{-1}\left(\frac{E}{\hbar\omega}\right)^{\frac{1}{2}} \quad (3)$$

where, $f_0(E)$ is the Fermi-Dirac distribution, $n(\omega)$ is the Bose-Einstein statistics, ω is the dominant optical phonon frequency calculated using Phonopy[12] (corresponding to the highest phonon energy at the G-point), ε_∞ is the high-frequency dielectric constant, and ε_s is the static dielectric constant. The parameters ε_∞ and ε_s were computed using the density functional perturbation theory (DFPT) method implemented in VASP.

Finally, the total carrier relaxation time τ can be determined based on the Mathiessen's law as equation (4)[13] by assuming that the above scattering processes are independent, and the average relaxation time is shown as follows[14]:

$$\frac{1}{\tau(T,\mu)} = \frac{1}{\tau_{ac}} + \frac{1}{\tau_{imp}} + \frac{1}{\tau_{polar}} \quad (4)$$

References:

1. Filippetti A. Mattoni A, Caddeo C, et al. Low electron-polar optical phonon scattering as a fundamental aspect of carrier mobility in methylammonium lead halide $CH_3NH_3PbI_3$ perovskites. *Phys Chem Chem Phys* **2016,** *18* (22), 15352-62.
2. Xi J, Long M, Tang L, et al. First-principles prediction of charge mobility in carbon and organic nanomaterials. *Nanoscale* **2012,** *4* (15), 4348-4369.
3. Tang L, Long M, Wang D, et al. The role of acoustic phonon scattering in charge transport in organic semiconductors: a first-principles deformation-potential study. *Science in China Series B: Chemistry* **2009,** *52* (10), 1646-1652.
4. Wang D, Shi W, Chen J, et al. Modeling thermoelectric transport in organic materials. *Phys Chem Chem Phys* **2012,** *14* (48), 16505-16520.
5. Wang D, Tang L, Long M, et al. First-principles investigation of organic semiconductors for thermoelectric applications. *J Chem Phys* **2009,** *131* (22), 224704.
6. Lu Y B, Kong X, Chen X, et al. Piezoelectric scattering limited mobility of hybrid organic-inorganic perovskites $CH_3NH_3PbI_3$. *Sci Rep* **2017,** *7*, 41860.
7. Chattopadhyay D, Queisser H J. Electron scattering by ionized impurities in semiconductors. *Reviews of Modern Physics* **1981,** *53* (4), 745-768.
8. Krishnaswamy K, Himmetoglu B, Kang Y, et al. First-principles analysis of electron transport in $BaSnO_3$. *Physical Review B* **2017,** *95* (20), 205202.
9. Fröhlich H. Electrons in lattice fields. *Advances in Physics* **1954,** *3* (11), 325-361.
10. Anderson D R, Zakhleniuk N A, Babiker M, et al. Polar-optical phonon-limited transport in degenerate GaN-based quantum wells. *Physical Review B* **2001,** *63* (24), 245313.
11. Sztein A, Haberstroh J, Bowers J E, et al. Calculated thermoelectric properties of $In_xGa_{1-x}N$, $In_xAl_{1-x}N$, and $Al_xGa_{1-x}N$. *Journal of Applied Physics* **2013,** *113* (18), 183707.
12. Togo A, Oba F, Tanaka I. First-principles calculations of the ferroelastic transition between rutile-type and $CaCl_2$-type SiO_2 at high pressures. *Physical Review B* **2008,** *78* (13), 134106.
13. Dugdale J S, Basinski Z S. Mathiessen's rule and anisotropic relaxation times. *Physical Review* **1967,** *157* (3), 552-560.
14. Yu D, Zhang Y, Liu F. First-principles study of electronic properties of biaxially strained silicon: effects on charge carrier mobility. *Physical Review B* **2008,** *78* (24), 245204.